ELSEVIER

Journal of Chromatography A, 831 (1999) 89–104

JOURNAL OF CHROMATOGRAPHY A

Advances in the theory of particle size distributions by field-flow fractionation
Outlet and apparent polydispersity at constant field

Mark R. Schure

Theoretical Separation Science Laboratory, Rohm and Haas Company, 727 Norristown Road, Spring House, PA 19477, USA

Abstract

A general equation for the apparent polydispersity is derived for the most common of the field-flow fractionation (FFF) techniques. The apparent polydispersity is the polydispersity that appears from the analysis of a monodisperse colloid sample if zone broadening is not removed from the calculated particle size distribution. Flow and electrical FFF are predicted to exhibit three-times the apparent polydispersity of sedimentation FFF for particle size analysis. Using a similar theoretical approach, the outlet response (bandpass filter function) of an FFF experiment is derived for a uniform number density of injected particle diameters. It is found that the bandpass filter function can be closely approximated by the same equations as that given for the apparent polydispersity.

Keywords: Field-flow fractionation; Particle size distribution; Apparent polydispersity; Polydispersity; Outlet response; Bandpass filter function

1. Introduction

Field-flow fractionation (FFF) methods are extremely useful in the characterization of colloidal and polymeric materials by providing particle sizing and molecular weight analysis for the colloid and polymer scientist. These analysis techniques have recently been augmented by the use of detectors such as the multi-angle laser light scattering (MALLS) detector [1–8] allowing for the evaluation of the particle size or polymer molecular weight independent of the FFF theory [9,10] that has been developed and refined for many years. The use of an FFF apparatus as a ''sorting'' device prior to detection should create a relatively narrow dispersity population of colloid or polymer in the detector flow cell. This should increase the accuracy of the detector and allow averages to be detected and accumulated for total size or molecular weight distribution analysis.

In a recent paper [6] it was shown how colloidal particles of both narrow and medium polydispersity could be quantitatively sized by flow FFF coupled to an on-line MALLS detector. If one examines the resulting temporal fractograms of these particles with a simple detector, for example the scattering amplitude at the 90° angle, the width of the fractograms are not indicative of the true particle size distributions [6]. This is due to the fact that non-equilibrium zone broadening is inherent in the resulting fractionator signal so that even a monodisperse particle causes a relatively broad signal to emerge from the fractionation process.

If the temporal signal of the fractionator is used to construct a particle size distribution for monodisperse and medium dispersity particles without de-

0021-9673/99/$ – see front matter
PII: S0021-9673(98)00560-3

convolution of the zone broadening [11,12], the size distribution will artificially reflect this broadening and not the true particle population [12]. This artifact has been previously referred to as ''apparent polydispersity'' [12]. The apparent polydispersity is defined [12] as the artifactual polydispersity that is quantitated in a size distribution measurement when a monodisperse colloid is fractionated and the zone broadening due to non-equilibrium processes is not removed through computer methods. The apparent polydispersity was previously studied for sedimentation FFF [12] where the high selectivity of this FFF technique keeps the apparent polydispersity quite low for all but the lowest levels of particle retention.

A closely related problem is to quantitate the polydispersity that an FFF technique presents to the detector at any instant, given an injection of a uniform distribution of particle sizes or molecular masses. This gives a measure of the separation efficacy which is useful in accessing the actual sample which is delivered to a detector capable of determining the particle size, such as a MALLS detector. This is important because the light scattering detector can bias the resulting size distribution if the incoming particle stream is too disperse. We will present this type of analysis in a later paper [13] where optical calculations based on the Mie theory of scattering [14,15] are used to simulate the MALLS process given the polydisperse particle populations at the fractionator outlet which are derived in this paper.

The production of narrow dispersity samples that are present at any temporal instant in the fractionator outlet is similar to the stationary time process of an electrical bandpass filter function in that the fractionator should ideally pass only one particle size or molecular weight at any instant of time. This is analogous to an ideal or perfect electrical bandpass filter which should pass only one unique frequency.

In this paper we focus on the comparison of the apparent polydispersity between the various FFF techniques using a generalization of theory previously developed for sedimentation FFF [12]. This is useful because particle sizing using other fractionation techniques besides sedimentation FFF, for example flow and electrical FFF, are becoming more popular. In addition, only a fraction of these FFF instruments are used with a MALLS detector so the issue of comparing the apparent polydispersity from the flow and electrical FFF techniques with sedimentation FFF is quite important and revealing. By a simple extension of the theory for particles, the apparent polydispersity can be used to describe the analysis of polymer molecular weights by thermal FFF.

Furthermore, numerical methods and theoretical analysis will be described which can be used to estimate the instantaneous bandpass function of an FFF experiment. This bandpass function will be compared with the apparent polydispersity and will be found to be nearly equal. The rationale for this agreement lies within the mathematics of convolution processes, as will be demonstrated. Finally, it will be shown how the particle size distribution of fractionated samples collected for a finite duration from an FFF apparatus can be calculated.

2. Results and discussion

2.1. Apparent polydispersity of particles

In what follows, the standard treatment of ideal Brownian particle FFF is used [10]. The approximations inherent in this theory include the absence of steric effects, particle–particle and particle–wall interactions and concentration effects. Furthermore, the aspect ratio of the channel is assumed to be large enough that edge effects are absent [10].

In FFF the polydispersity contribution to the length-based peak variance, σ_p^2, is given as [16]:

$$\sigma_p^2 = \left(\frac{dz}{dd}\right)^2 \sigma_d^2 \tag{1}$$

where z is the axial distance down the channel, d is the particle diameter, and σ_d^2 is the variance of the particle diameter number density function. Using the chain rule it has been previously shown that [16]:

$$\sigma_p^2 = \left(\frac{dz}{dR}\frac{dR}{d\lambda}\frac{d\lambda}{dd}\right)^2 \sigma_d^2 \tag{2}$$

where R and λ are the well known retention ratio (equal to the ratio of void time t_0 to retention time t_r) and non-dimensional mean layer thickness, respectively [9,10,16]. The first term, dz/dR, is simply L/R, where L is the channel length. The middle term

will be manipulated shortly. The last term can be easily generalized as the theory of retention for electrical, flow and sedimentation FFF gives the mean layer thickness as [9,10]:

$$\lambda = \frac{\lambda'}{d^n} \tag{3}$$

where n is an integer and λ' is a lumped term which is unique for each subtechnique of FFF mentioned above. It is known that n is exactly equal to the values of 1, 1 and 3 for electrical [17], flow [18], and sedimentation FFF [19], respectively. These are also the values of the asymptotic selectivities, S_d of each FFF subtechnique defined as:

$$S_d = \left| \frac{\mathrm{d} \log t_r}{\mathrm{d} \log d} \right| \tag{4}$$

The last derivative term, $\mathrm{d}\lambda/\mathrm{d}d$, can be written as:

$$\frac{\mathrm{d}\lambda}{\mathrm{d}d} = -n\frac{\lambda}{d} \tag{5}$$

Combining Eqs. (2) and (5) gives:

$$\sigma_p^2 = n^2 L^2 \left(\frac{\mathrm{d}R}{R}\right)^2 \left(\frac{\lambda}{\mathrm{d}\lambda}\right)^2 \left(\frac{\sigma_d}{d}\right)^2 \tag{6}$$

Further manipulation of Eq. (6) gives:

$$\sigma_p^2 = n^2 L^2 \left(\frac{\mathrm{d} \ln R}{\mathrm{d} \ln \lambda}\right)^2 \left(\frac{\sigma_d}{d}\right)^2 \tag{7}$$

The quantity σ_d/d is the relative polydispersity and figures highly in the following equations and treatments yet to come.

Note that $\mathrm{d} \ln R/\mathrm{d} \ln \lambda$ can be asymptotically reduced to unity in the limit as $R \to 0$. However, this approximation is not made because some of the results will be given at low retention (high R) and we want to preserve as much accuracy as possible in this region. This term is easily calculated using derivative estimation of the polynomial interpolated logarithm values via Lagrange interpolation [20] and is equal to 0.9226 for $R=0.2$ and 0.9642 for $R=0.1$. Some approximations of $\mathrm{d} \ln R/\mathrm{d} \ln \lambda$ are known in the low retention (high R) region [21] but these will not be considered further because of the ease in which this term can be computed using numerical methods.

Eq. (7) gives the zone variance, σ_p^2, as a function of the FFF experimental variables and the sample variables σ_d and d. Therefore, if $\sigma_d = 0$ then $\sigma_p = 0$ as expected. However, due to non-equilibrium zone broadening, which has its origins in diffusion, a monodisperse particle will still give a fractogram showing broadening. If the broadening due to a monodisperse particle population is equated to σ_d through σ_p, a false value of σ_d will be calculated. This is exactly what we want to do here as this tells us about the inherent quality of the calculated particle size distribution.

The final step for this treatment is to equate the length-based zone variance due to non-equilibrium, σ_{ne}^2, with the length-based zone variance due to polydispersity, σ_p^2. We then solve for the apparent polydispersity, σ_d/d, that would result when a monodisperse particle causes zone broadening and this broadening is interpreted as having its origins in polydispersity.

From FFF theory [10,22,23]:

$$\sigma_{ne}^2 = H_{ne} L = \frac{\chi w^2 L \langle v \rangle}{D} \tag{8}$$

where H_{ne} is the plate height due solely to non-equilibrium, w is the channel thickness, $\langle v \rangle$ is the average fluid velocity in the channel, D is the diffusion coefficient, and χ is the non-dimensional non-equilibrium parameter [23] equal to $24\lambda^3$ in the limit as $R \to 0$.

The diffusion coefficient can be further equated to the fundamental variables for dilute colloidal materials through the Stokes–Einstein equation [24]:

$$D = \frac{k_B T}{3\pi\eta d} \tag{9}$$

where k_B is Boltzmann's constant, T is temperature, and η is the solution viscosity.

The plate height due to molecular diffusion is not included in this treatment because it is generally negligible in the study of colloidal materials. Hence, equating Eqs. (7) and (8) and substituting Eq. (9) for D yields:

$$\left(\frac{\sigma_d}{d}\right)_{ap} = \frac{w}{n}\left(\frac{\mathrm{d} \ln \lambda}{\mathrm{d} \ln R}\right)\left(\frac{3\pi\chi\eta\langle v \rangle d}{L k_B T}\right)^{1/2} \tag{10}$$

Inspection of Eq. (10) reveals that the sedimentation FFF technique should have one-third the appar-

ent polydispersity of the other FFF techniques because n is in the denominator. Furthermore, reduction in the flow-rate through $\langle v \rangle$ will not help much in reducing the apparent polydispersity because of the one-half power dependence.

Eq. (10) is evaluated under a number of conditions in Fig. 1 as a function of the retention ratio R using n equal to 1 for electrical and flow FFF and 3 for sedimentation FFF. As can be seen from Fig. 1, the apparent polydispersity is rather low for sedimentation FFF, as was previously given in exactly the same form of representation in Ref. [12]. However, we now see that these other forms of FFF give rather high apparent polydispersities. For example at $R=0.1$, or 10 column volumes of retention, a 0.2 μm diameter particle in electrical or flow FFF appears to give $\sigma_{ap} \approx 0.02$ μm where σ_{ap} is the standard deviation of the apparent particle size density function. At first this does not appear to be that large but if one plots this as a Gaussian density function one realizes that the baseline of the function at the $\pm 3\sigma$ level extends from 0.14 μm to 0.26 μm, which is large in typical colloidal particle applications. This is contrasted with sedimentation FFF where under the same conditions except for $n=3$, one third the zone broadening is obtained. Hence $\sigma_{ap} \approx 0.0066$ μm which gives a baseline of the Gaussian density function at the $\pm 3\sigma$ level starting at 0.18 μm and ending at 0.22 μm. Therefore, particle characterization with sedimentation FFF gives less apparent polydispersity values than electrical or flow FFF.

One can compare the various FFF techniques in a more graphic way by plotting the broadened and unbroadened size distributions for monodisperse particles. These are shown in the following figures and produced in a manner similar to that described in Ref. [12], except for the application of the theory which uses $n=1$ or $n=3$. Furthermore, it is assumed that a monodisperse particle population will broaden in the time domain according to a Gaussian density. This is accurate for $R<0.2$ as determined by Monte Carlo simulations [25]. However, for the work described in this study Gaussian broadening will be assumed to occur throughout the elution range. All of the calculations in this paper use computer programs written with 64 bit arithmetic precision. The number of significant digits in the independent variables reported here is at least good to 10 places but for simplicity we report these with just enough digits to indicate the number. The dependent (calculated) variables are reported with four places of precision for convenience.

This comparison is shown in Figs. 2 and 3. In both figures, λ' is calculated for $n=1$ and $n=3$ given the retention ratio, R_{min}, at the largest particle diameter.

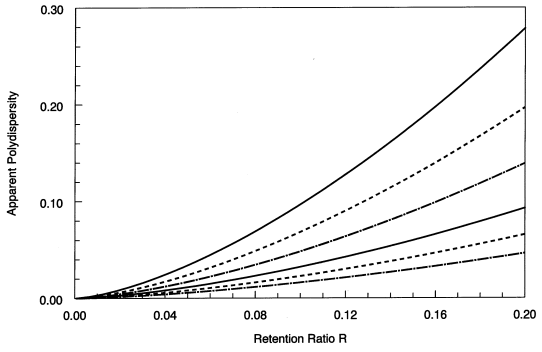

Fig. 1. The apparent polydispersity, $(\sigma_d/d)_{ap}$, as a function of the retention ratio R for $n=1$ (the top three curves) and $n=3$ (the bottom three curves) for the particle diameters of 0.2 μm (—), 0.1 μm (- - -) and 0.05 μm (– · –). The flow-rate $F=1$ ml min^{-1}, $L=60$ cm, $w=0.0127$ cm, $\langle v \rangle = 0.656$ cm s^{-1}, $T=296$ K and $\eta=0.01$ Poise.

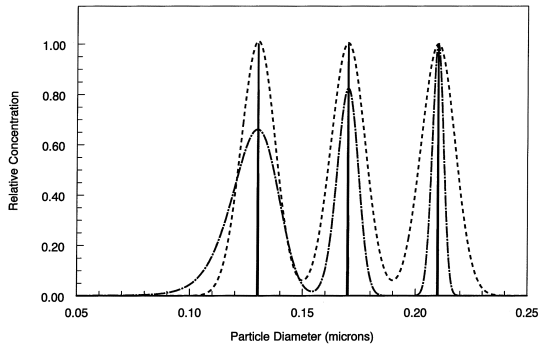

Fig. 2. The broadened (- - -) for $n=1$, broadened (– · –) for $n=3$, and the original (—) particle size distributions from three monodisperse particle populations with diameters of 0.13, 0.17 and 0.21 μm. The retention ratio R is chosen to be 0.05 for the largest mean particle size. The R values for the smallest mean diameter are 0.1991 for $n=3$ and 0.07991 for $n=1$ and the R values for the middle mean diameter are $R=0.09281$ for $n=3$ and $R=0.06151$ for $n=1$. Other conditions as in Fig. 1. The results are normalized so that the number concentrations at the largest particle diameter peak are equal.

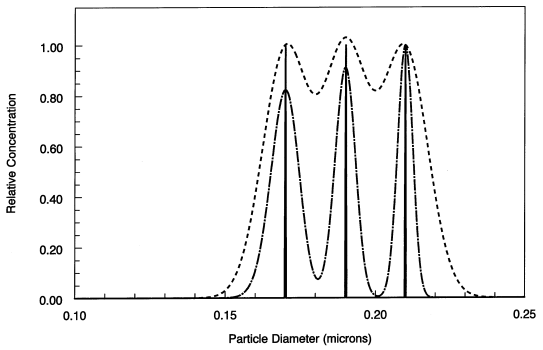

Fig. 3. The broadened (- - -) for $n=1$, broadened (– · –) for $n=3$, and the original (—) particle size distributions from three monodisperse particle populations with diameters of 0.17, 0.19 and 0.21 μm. The retention ratio R is chosen to be 0.05 for the largest mean particle size. The R values for the smallest mean diameter are 0.09281 for $n=3$ and 0.06151 for $n=1$ and the R values for the middle mean diameter are $R=0.06710$ for $n=3$ and $R=0.05516$ for $n=1$. Other conditions are as in Fig. 1. The results are normalized so that the number concentrations at the largest particle diameter peak are equal.

The value of R_{min} used in these studies is noted in the figure captions. The constraint of keeping R_{min} constant while varying n forces the other particle diameters to be compared at different values of R which is a biased comparison, but nonetheless informative. For example in Fig. 2, particle diameters of 0.13 μm, 0.17 μm and 0.21 μm are shown for $n=1$ and $n=3$. For the largest particle diameter and most retained peak, very little extraneous broadening is shown for the case of $n=3$, however, the $n=1$ case shows the expected larger amount of broadening. For this peak both the $n=1$ and $n=3$ case are calculated at $R=0.05$, allowing for an unbiased comparison. However, the retention of the peaks at 0.13 μm are calculated at $R=0.1991$ and $R=0.07991$ for $n=3$ and $n=1$, respectively and the peaks at 0.17 μm are calculated at $R=0.09281$ and $R=0.06151$ for $n=3$ and $n=1$, respectively. Because of these differences in R, the $n=3$ result actually appears to be more broadened than the $n=1$ result for the smallest particle diameter. As shown in Fig. 1, the apparent polydispersity for $n=3$ and $R=0.2$ for $d\geq 0.2$ μm is larger than the case of $n=1$ and $R=0.08$. Hence, it is no surprise that for constant field strength these choices of particle diameters indicates that the $n=1$ result is better in terms of least broadening of the particle size distribution of the smallest particle. It is easily seen though, for the two larger particle sizes, that the $n=3$ result shows less broadening of the calculated particle size distribution.

For three particles with closer diameters, the superiority of the $n=3$ result is further evident from Fig. 3. The retention ratios of the two smaller size particles are $R=0.09281$ and $R=0.06710$ for $n=3$ and $R=0.06151$ and $R=0.05516$ for $n=1$. However, in this case the superiority of the $n=3$ result which clearly shows three distinct distributions is contrasted with the $n=1$ case where the three distributions are barely visible.

These results highlight the observation that as n increases, the need for field programming also increases. This is because higher n techniques will spread the results of constant field fractograms farther over the elution space. These results indicate that it is easier to get a wider range of particle sizes fractionated with low n techniques although at lower resolution. For techniques other than FFF techniques where n is smaller than unity, the whole experiment can be conducted in a short time; the problem is that one usually sacrifices resolution here and the particle fractionation is carried out with lower quality.

2.2. Apparent polydispersity of polymers

We have examined the apparent polydispersity concept for colloidal particles. We can use exactly the same concepts for the analysis of the apparent polydispersity of polymers where molecular weight, not particle diameter, is the variable of interest. Similar to Eqs. (1) and (2) we denote the peak variance due to polydispersity as:

$$\sigma_p^2 = \left(\frac{dz}{dM}\right)^2 \sigma_M^2 \tag{11}$$

where M is the molecular weight of the polymer and σ_M^2 is the variance of the molecular weight number density function. This can be expanded in a manner similar to Eq. (2) as:

$$\sigma_p^2 = \left(\frac{dz}{dR}\frac{dR}{d\lambda}\frac{d\lambda}{dM}\right)^2 \sigma_M^2 \tag{12}$$

The molecular weight of polymers can be obtained in principle using a number of different FFF tech-

niques, however, we focus here on thermal FFF. One can use thermal FFF for particle sizing [26] although this application is not completely understood. In thermal FFF the molecular weight dependence on retention through λ is expressed empirically [27] as:

$$\lambda = \frac{\lambda'}{M^{S_M}} \tag{13}$$

where S_M is the molecular weight-based selectivity defined as:

$$S_M = \left| \frac{d \log t_r}{d \log M} \right| \tag{14}$$

Eq. (5) is now written for thermal FFF as:

$$\frac{d\lambda}{dM} = -S_M \frac{\lambda}{M} \tag{15}$$

Combining Eqs. (12) and (15) and utilizing the previous results for the first two derivative terms in Eq. (12) gives:

$$\sigma_p^2 = S_M^2 L^2 \left(\frac{d \ln R}{d \ln \lambda} \right)^2 \left(\frac{\sigma_M}{M} \right)^2 \tag{16}$$

The final step is to equate the broadening due to non-equilibrium processes, σ_{ne} from Eq. (8), with Eq. (16) to obtain the apparent polydispersity in molecular weight. This then gives:

$$\left(\frac{\sigma_M}{M} \right)_{ap} = \frac{w}{S_M} \left(\frac{d \ln \lambda}{d \ln R} \right) \left(\frac{\chi \langle v \rangle}{LD} \right)^{1/2} \tag{17}$$

This gives a general equation for the molecular weight-based apparent polydispersity. For the case of thermal FFF the diffusion coefficient is typically specified in a semi-empirical form [28] that includes the molecular weight and temperature dependence:

$$D = \frac{1}{M^b} \exp (A + C/T) \tag{18}$$

where $A = -3.6851$, $b = 0.552$ and $C = -1360$ for polystyrene in ethyl benzene [28]. Note that T in Eq. (18) is typically the temperature at the mean layer height. The cold wall temperature in thermal FFF is fairly close to this and may be substituted with little error. In addition, $S_M \approx b$ [27]. Substituting Eq. (18) into Eq. (17) yields:

$$\left(\frac{\sigma_M}{M} \right)_{ap} = \frac{w}{S_M} \left(\frac{d \ln \lambda}{d \ln R} \right) \left(\frac{\chi \langle v \rangle M^b}{L \exp (A + C/T)} \right)^{1/2} \tag{19}$$

Hence, the apparent molecular weight polydispersity can be formulated in a similar manner to that for the other FFF techniques where colloidal particle size was previously investigated.

Evaluation of the apparent polydispersity, σ_M/M, as a function of the retention ratio R for a number of different molecular weights of polystyrene in ethyl benzene is shown in Fig. 4 as would be analyzed by thermal FFF. We show higher R values here, as opposed to Fig. 1, because in thermal FFF one can get more useful information at higher R values than from the other FFF techniques where colloidal particles are fractionated. This is due to the faster transverse movement of polymers within the zone due to larger diffusion coefficients as contrasted with colloidal particle fractionation where smaller diffusion coefficients are encountered.

As is evident from Fig. 4, lower R values must be used to avoid very high apparent polydispersities for monodisperse polymers and for high-molecular-weight materials. However, comparison of Figs. 1 and 4 at constant R reveals that thermal FFF appears to have similar apparent polydispersities to that of flow FFF, although the comparison is biased because we are comparing particles and polymers.

We have shown how simple equations can be used

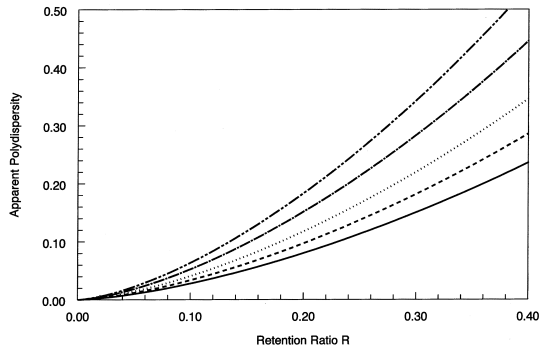

Fig. 4. The apparent polydispersity, $(\sigma_M/M)_{ap}$, as a function of the retention ratio R for thermal FFF of polystyrene in ethyl benzene. The molecular weights used in the calculation are: 1 000 000 (– · · –), 500 000 (– · –), 200 000 (· · ·), 100 000 (- - -) and 50 000 (—). Other conditions as in Fig. 1.

to contrast the apparent polydispersity quantity from the various FFF techniques. In that regard, a convenient comparison can be made between these FFF techniques with regards to the fidelity of particle sizing when monodisperse and narrow dispersity materials are to be characterized. Overall, the magnitude of the apparent polydispersity is fairly low, especially when experiments are run at field strengths which yield retention ratios less than 0.1. Under this constraint, the FFF techniques are predicted to yield apparent polydispersities below 5 to 10% without deconvolution. This is quite good and provides a basis for evaluating the quality of particle sizing using this set of techniques. The apparent polydispersity approach can also be applied to other separation systems, for example size-exclusion chromatography (SEC) and capillary hydrodynamic fractionation (CHDF). Thus, the apparent polydispersity concept provides an alternative to other performance metrics such as the fractionating power [29,30] and the specific resolution factor [31] for characterizing the efficacy of particle and polymer fractionation systems.

2.3. Time–size matrix

For the theoretical treatment that follows a convenient formulation can be obtained by using a matrix which expresses the temporal concentration profile in each column for a given particle diameter. This time–size number concentration matrix, $\mathbf{A}_{ij}$, is composed of m rows $i \in 1{:}m$ at time t_i and k columns $j \in 1{:}k$ at particle diameter d_j. The matrix is synthesized in the following manner. First, the largest particle diameter, $d_{\max}$, in the injected particle size density function is specified along with the retention ratio minimum, $R_{\min}$, of the largest particle. Next, $\lambda_{\min}$ is calculated from $R_{\min}$ using a simple $R \rightarrow \lambda$ inversion algorithm [32]. This inversion algorithm utilizes interpolation on a look-up table which is produced from the well-known forward relationship $\lambda \rightarrow R$ by:

$$R = 6\lambda \coth\left(\frac{1}{2\lambda}\right) - 12\lambda^2 \tag{20}$$

From $\lambda_{\min}$ and the corresponding $d_{\max}$, Eq. (3) is used to calculate λ' when n is specified according to the desired FFF technique. The particle size number density function used here is uniform with equal numbers of particles for $0 < d \leq d_{\max}$.

The matrix is synthesized by calculating Gaussian temporal densities at each particle diameter d_j. Hence, each of the k diameters is sequentially chosen and represented as a delta function density of particle diameter, $\delta(d_j')$, the corresponding transformation of $d_j' \rightarrow \lambda \rightarrow R \rightarrow t_j'$ is made, and the temporal zone broadening allows the construction of the time–size matrix as:

$$\mathbf{A}_{ij} = \frac{1}{\sqrt{2\pi}\sigma_j} \exp\left[\frac{-(t_i - t_j')^2}{2\sigma_j^2}\right] \tag{21}$$

In Eq. (21) σ_j is the temporal Gaussian standard deviation calculated at each particle diameter d_j. The quantity σ_j is calculated as follows.

The plate height in FFF is dominated by non-equilibrium (Taylor dispersion) processes. The plate height contribution from non-equilibrium, H_{ne}, is obtained by modifiying Eq. (8) and is given as:

$$H_{\text{ne}} = \frac{\chi w^2 \langle v \rangle}{D} \tag{22}$$

The plate height is determined from experiment as:

$$H = L\left(\frac{\sigma^2}{t^2}\right) \tag{23}$$

and equating Eqs. (22) and (23) and rearranging gives the result that:

$$\sigma_j^2 = \frac{\chi w^2 \langle v \rangle t_j'^{\,2}}{LD} \tag{24}$$

Substituting the Stokes–Einstein equation given in Eq. (9) into Eq. (24) gives:

$$\sigma_j^2 = \frac{3\pi\chi w^2 \langle v \rangle t_j'^{\,2} \eta d_j}{Lk_{\text{B}}T} \tag{25}$$

noting that χ is evaluated at the λ which corresponds to t_j' and d_j.

The construction of $\mathbf{A}_{ij}$ then allows the determination of the particle size density function at any time t_i. The particle size density function is just the row of $\mathbf{A}_{ij}$ at t_i which we denote as $N(d_j)|_{t_i}$, the particle diameter number density at constant time t_i. Furthermore, the particle diameter density of a

collected aliquot which is collected between times t_i and t_{i+p} is simply:

$$N(d_j)|_{t_i}^{t_{i+p}} = \int_{t_i}^{t_{i+p}} \mathbf{A}_{ij} dt \quad (26)$$

or given in a less accurate discrete form:

$$N(d_j)|_{t_i}^{t_{i+p}} = \sum_{i}^{i+p} \mathbf{A}_{ij} \quad (27)$$

The signal from a MALLS detector or a UV chromatographic detector employed as a tubidity detector can be given as a function of time as:

$$f(t_i, \theta) = \sum_{j=1}^{k} \mathbf{A}_{ij} C_j(\theta) \quad (28)$$

where $f(t_i, \theta)$ is the detector signal at time t_i and scattering angle θ and $C_j(\theta)$ is the extinction coefficient which is dependent on the particle diameter, the particle and solution refractive indices, and the incident scattering angle [14,15].

The time–size matrix can be evaluated on personal computers with very short computation times. The matrix size of 1000 by 500 is used throughout this paper.

2.4. Bandpass function

The time–size matrix for FFF systems which have $n=1$ in Eq. (3), for example flow and electrical FFF, is shown in Fig. 5. The time–size matrix for $n=3$ which is characteristic of sedimentation FFF is shown in Fig. 6. The dark area of these matrices is where the number concentration of particles is contained. The white area represents particle concentrations at least 1000-times less than that in the center regions of the dark areas.

As can be seen from these two figures, the $n=3$ case in Fig. 6 has much better (narrower) bandpass characteristics after a few minutes ($t_0 \approx 1.5$ min) than that shown in Fig. 5 for the $n=1$ case. The $n=1$ case in Fig. 5 also appears to be much more constant in bandpass across the elution range than does the $n=3$ case shown in Fig. 6. As was discussed earlier, at constant field the $n=3$ broadening is large in the early stages of the fractogram compared with the broadening in the later ($R<0.2$) stages of the fractogram. This result again demonstrates the critical need for field programming with sedimentation FFF and also illustrates the extremely large broadening that takes place near the void peak for smaller particles. This can be somewhat compensated experimentally by running at high initial field; we will consider this aspect in a later paper in this series

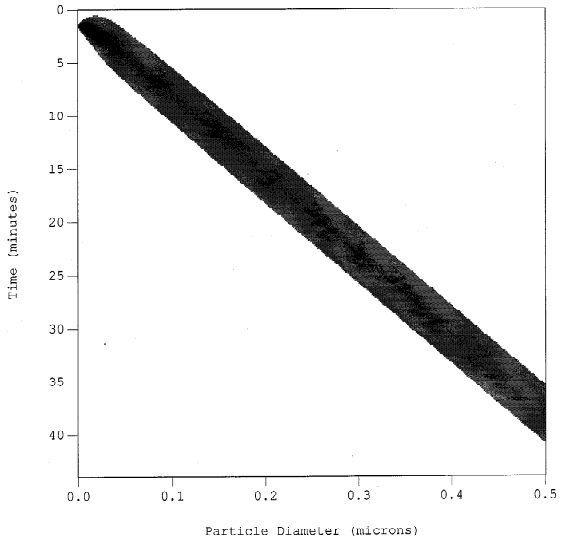

Fig. 5. The time–size matrix for $n=1$, $R_{min}=0.04$, $d_{max}=0.5$ μm, $T=298$ K, $w=0.0127$ cm, $F=1$ ml min^{-1}, $\langle v \rangle = 0.656$ cm s^{-1}, and $\eta=0.01$ Poise.

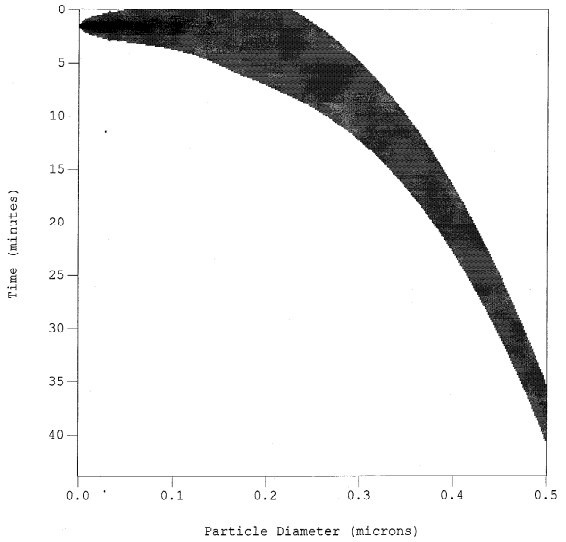

Fig. 6. The time–size matrix for $n=3$. All other parameters as in Fig. 5.

which examines the bandpass function with field programming for both $n=1$ and $n=3$ systems [33].

Although the mathematical analysis has stated that Gaussian broadening occurs in the time domain, a peak shape analysis of the broadening amplitude in the particle diameter domain is easily accomplished by taking row slices of the time–size matrix which gives $N(d_j)|_{t_i}$. These slices are shown in Fig. 7. As can be seen from this figure, all zones except for the earlier eluting zones of the $n=3$ calculations appear to be very close to Gaussian in shape. The $n=1$ zones appear to be mostly constant in width, as was seen in Fig. 5. The later eluting zones for $n=3$ are distinctively less broad than the zones for the $n=1$ case, as was also seen from Figs. 5 and 6.

2.5. Outlet and apparent polydispersity

Through the use of moment analysis [34] it is an easy task to take the time–size matrix, $\mathbf{A}_{ij}$, and plot the standard deviation of the particle diameter density at constant time, $\sigma_d|_{t_i}$, as a function of the average particle diameter, $\bar{d}|_{t_i}$. This is mathematically expressed as:

$$\bar{d}|_{t_i} = \frac{\int_0^{d_{max}} \mathbf{A}_{ij} d_j \mathrm{d}d_j}{\int_0^{d_{max}} \mathbf{A}_{ij} \mathrm{d}d_j} \tag{29}$$

and

$$\sigma_d|_{t_i} = \sqrt{\frac{\int_0^{d_{max}} \mathbf{A}_{ij}\left(d_j - \bar{d}|_{t_i}\right)^2 \mathrm{d}d_j}{\int_0^{d_{max}} \mathbf{A}_{ij} \mathrm{d}d_j}} \tag{30}$$

Additionally, we can make the dependent variable non-dimensional, facilitating easier comparison, by taking the ratio of $\sigma_d|_{t_i}$ to $\bar{d}|_{t_i}$ as a function of $\bar{d}|_{t_i}$ as shown in Fig. 8. This ratio will be referred to as the outlet polydispersity.

Four curves are shown in Fig. 8. We start our comparison with the curves derived from Eqs. (29) and (30) which show the outlet polydispersity of the time–size matrix given for $n=1$ and $n=3$ in Figs. 5 and 6. In both cases the outlet polydispersity decreases to levels below 0.1 at the higher particle diameters but for both cases the outlet polydispersity is quite high at lower particle diameters. The information in Fig. 8 is contained in Figs. 5 and 6 but is simply presented in a different way in Fig. 8.

Also shown in Fig. 8 is the comparison of the outlet polydispersity with the apparent polydispersity given in Eq. (10). Eq. (10) has an implicit relationship in λ; i.e., a particle diameter d is chosen and then λ is obtained from Eq. (3) to give χ and R. We utilize $\bar{d}|_{t_i}$ from Eq. (29) as d in Eq. (10).

The apparent polydispersity is seen to be an excellent fit to the outlet polydispersity for $n=1$ throughout the elution range and for the $n=3$ result in the higher retention region. This agreement was not expected. To further investigate this agreement

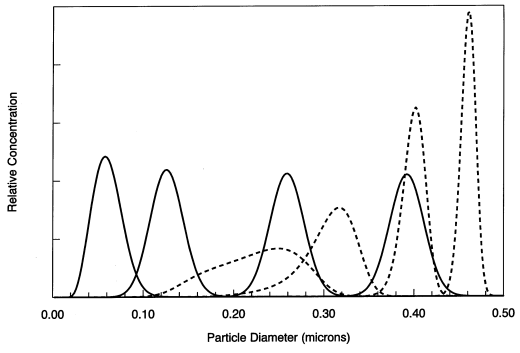

Fig. 7. The diameter distribution at various time slices for both $n=1$ (—) and $n=3$ (- - -). The times are 5, 10, 20 and 30 min for both sets of results and are in order of smallest to largest particle diameter. The area under all of the density functions is equal. The conditions are as in Figs. 5 and 6.

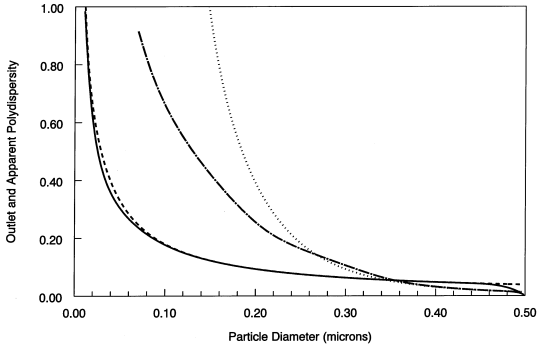

Fig. 8. The outlet polydispersity for $n=1$ (—) and for $n=3$ (– · –) plotted along with the apparent polydispersity for $n=1$ (- - -) and $n=3$ (· · ·) as a function of the diameter calculated using Eq. (29). The conditions are as in Figs. 5 and 6.

between two seemingly unrelated quantities, the results of Fig. 8 can be plotted with an independent variable axis which more resembles the elution experiment. Hence, in Fig. 9 the outlet and apparent polydispersities are plotted as a function of the number of column volumes which is proportional to time and equal to t_r/t_0. The number of column volumes is the reciprocal of R.

The agreement now appears to be much better and the deviation occurs primarily below five column volumes ($R>0.2$) where it is known that the retention theory and zone broadening theory tend to produce inaccurate results [25]. However, the assumption of Gaussian zones at these low retention levels is certainly the largest source of error in synthesizing the time–size matrix. The error is severe enough in this region that with small particle sizes there is a finite probability that particles elute at zero time because of error in σ_j at very small retention. This is shown very clearly in Fig. 6. Other sources of error exist but are of minor considerations in this comparison. Hence, both the analytical theory for polydispersity given in Eq. (10) and the time–size matrix have large errors in the low retention region. These errors are compounded in the $n=3$ case because so much of the small particle sizes are contained in this region. The disagreement at higher retention is certainly due to the truncation of the particle size density at d_{max}.

The outlet polydispersity and the apparent polydispersity appear to be nearly equal in the medium and high retention region. The reason for this is as follows. As seen from Fig. 10, the development of the apparent polydispersity concept can be represented as a series of operations on density functions. First, a delta function diameter density, $\delta(d_j')$, is converted into the time domain using the transformation $d_j' \rightarrow t_j'$, giving $\delta(t_j')$ as shown in Fig. 10. Next, this density is broadened through convolution with a Gaussian function. This step is written as:

$$N(t_i)|_{d_j'} = \frac{1}{\sqrt{2\pi}\sigma_j} \exp\left[\frac{-(t_i - t_j')^2}{2\sigma_j^2}\right] \tag{31}$$

where $N(t_i)|_{d_j'}$ is the relative number concentration which is similar to the columns in Eq. (21) and σ_j^2 is given by Eq. (25). Next, the time axis is converted back to the diameter axis using the transformation $t_i \rightarrow d_i$. This then gives a density function whose standard deviation could be obtained by moment analysis but is approximated analytically by σ_d in Eq. (10).

The development of the outlet polydispersity is

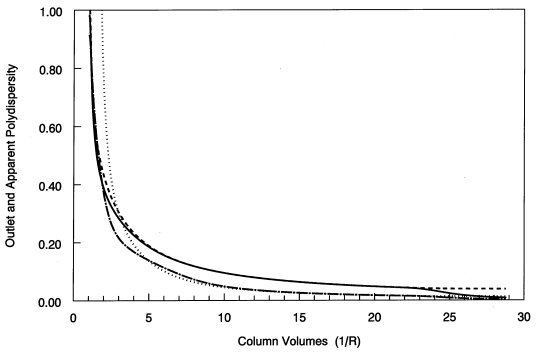

Fig. 9. The same results as in Fig. 8 except the independent variable axis is derived from the retention time axis and plotted as the number of column volumes.

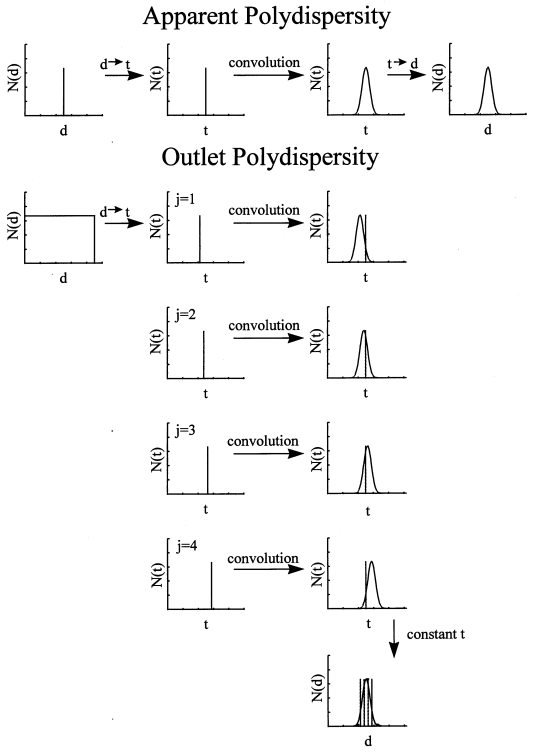

Fig. 10. The unit operations which show the calculation of the apparent polydispersity and the outlet polydispersity.

also shown in Fig. 10 as a series of operations on density functions. A uniform number density of diameters is chosen, as discussed previously. This density is represented as a series of finely spaced delta functions such that $\delta(d_j')$ equals unity for $0< d_j' \leq d_{max}$.

As shown in Fig. 10, individual delta functions are now placed on a temporal axis through the transformation $d_j' \rightarrow t_j'$ and labeled as $j=1, 2, 3, 4,...$ to show the breakdown of the uniform size density into a series of delta functions. The same temporal convolution operation is then performed as is contained in each column of $\mathbf{A}_{ij}$, as shown in Fig. 10. This results in a series of temporal Gaussian-based curves which have means and standard deviations which are dependent on the particle diameter d_j'.

The particle size density at the outlet is just the line shown in Fig. 10 at constant time, t_i, from which the diameter density is contributed from each individual temporal fractogram for $j=1, 2, 3, 4,...$; this is expressed as:

$$N(d_j)|_{t_i} = \frac{1}{\sqrt{2\pi}\sigma_j} \exp\left[\frac{-(t_i - t_j')^2}{2\sigma_j^2}\right] \quad (32)$$

noting that t_j' and σ_j are functions of d_j.

One can easily see that Eqs. (31) and (32) appear to be the same equation noting that Eq. (31) gives the number concentration as a function of time at constant diameter and Eq. (32) is the number concentration as a function of diameter at constant time. These equations are evaluated differently; in Eq. (31) σ_j and t_j' are constants while in Eq. (32) a different σ_j and t_j' are obtained at every value of the independent variable, d_j. Furthermore, in Eq. (31) t_i is not constant while in Eq. (32) t_i is constant.

For $n=1$ the mapping of $t_i \rightarrow d_i$ in Eq. (31) is approximately linear as will be shown below in Eq. (39). Furthermore, if σ_j is approximately constant for $n=1$, as it appears from Figs. 5 and 7 (it will be shown that σ_j is approximately constant for $n=1$ from theory given below), then $N(t_i)|_d$ in Eq. (31) should convert to $N(d_i)$ in a linear manner. In this case Eq. (31) will be linearly converted to $N(d_i)$ and agreement between the apparent and outlet polydispersity should differ at most by a constant factor. However, for the mapping of $t_i \rightarrow d_i$ when $n=3$ or in general when $n \neq 1$, the non-linear mapping of $t_i \rightarrow d_i$, as shown below in Eq. (39), should ensure that Eq. (31) cannot take on a one-to-one correspondence with the form of Eq. (32). In this case agreement between the apparent polydispersity and outlet polydispersity will occur only as a limiting process. Although this is not a rigorous proof that the apparent polydispersity and outlet polydispersity are not equivalent, the differences between the $n=1$ and $n=3$ cases viewed in Figs. 8 and 9 support the hypothesis that the $t \leftrightarrow d$ mappings must be linear and σ_j be constant to get nearly exact agreement.

The agreement between the outlet and apparent polydispersities is sufficient to allow the usage of the apparent polydispersity as an approximate analytical solution to the outlet polydispersity for constant field FFF, under medium to high retention conditions. This allows one to mathematically explain the observation shown in Fig. 5 that the particle size broadening, $\sigma_d|_{t_i}$, appears to be constant throughout most of the elution range for the $n=1$ case. This is accomplished as follows.

Using the approximations $\chi = 24\lambda^3$ and $d \ln \lambda / d \ln R = 1$ in Eq. (10) gives upon rearranging:

$$\sigma_d = \frac{6w}{n}\left(\frac{2\pi\eta\langle v\rangle}{Lk_BT}\right)^{1/2} (\lambda d)^{3/2} \quad (33)$$

Since the product $\lambda d = \lambda'$ when $n=1$, Eq. (33) can be written specifically for the $n=1$ case as:

$$\sigma_d = 6w(\lambda')^{3/2}\left(\frac{2\pi\eta\langle v\rangle}{Lk_BT}\right)^{1/2} \quad (34)$$

Eq. (34) shows the result that σ_d is independent of particle diameter and only dependent on column operating and geometric parameters for techniques such as flow and electrical FFF.

This is not the case for sedimentation FFF where $n=3$ and the $(\lambda d)^{3/2}$ term in Eq. (33) now becomes $(\lambda')^{1/2}\lambda$ so that:

$$\sigma_d = 2w\left(\frac{2\pi\eta\langle v\rangle\lambda'}{Lk_BT}\right)^{1/2} \lambda \quad (35)$$

Here σ_d is proportional to λ; this denotes that σ_d is proportional to d^{-3} and larger particles will have much smaller outlet σ_d as shown in Figs. 6 and 7. If the approximation $R = 6\lambda$, which is valid at high retention (low R), is utilized in Eq. (35) one

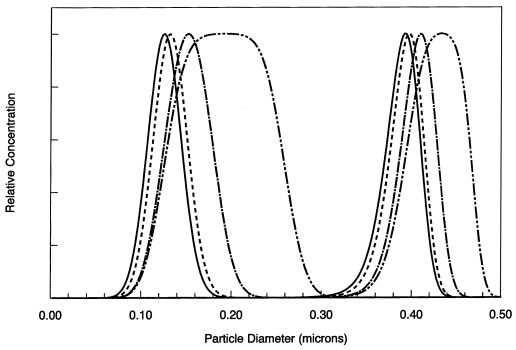

Fig. 11. The particle diameter density for various fraction collection accumulation times of 0 min (—), 1 min (- - -), 4 min (– · –), and 10 min (– · · –). The smaller diameter collections are with $n=1$ and start at 10 min. The larger diameter collections are with $n=3$ and start at 15 min. All other conditions as in Fig. 5.

produces the simple result for constant field FFF at $n=3$ that:

$$\sigma_d = \frac{wt_0}{3t_r}\left(\frac{2\pi\eta\langle v\rangle\lambda'}{Lk_BT}\right)^{1/2} \quad (36)$$

where it is seen that σ_d will be inversely proportional to the retention time t_r. Hence in flow and electrical FFF, the standard deviation (and variance) of the outlet particle diameter density function is predicted to be time invariant while for sedimentation FFF the standard deviation of the outlet particle diameter density function is predicted to be inversely proportional to time.

2.6. Fraction collection

The calculation of the outlet particle size density when the outlet particles are accumulated for a finite time period, for example during fraction collection, is accomplished through the use of Eq. (26) or Eq. (27). Examples of the particle size density functions from this accumulation process are shown in Fig. 11 where the accumulation time is varied. As seen from Fig. 11, the diameter density functions appear to be Gaussian in shape except for the two examples where 10-min accumulation times are used. Also seen from Fig. 11 is that the average diameter shifts to larger diameters as the accumulation time increases.

The moment analysis of these curves is given in Table 1. The first moment gives the centroid average diameter and the square root of the second moment gives the standard deviation of the size density function. In addition to the moment analysis, analytical equations can be derived which approximate the first moment and the standard deviation derived from the second moment. We derive these equations now.

The average value, $\bar{f}$, of a time-varying continuous function f(t), can be obtained between the temporal limits t_i and t_{i+p} as:

Table 1
Evaluation of the average diameter and standard deviation from the zone collection shown in Fig. 11

Collection time range (min)	$\bar{d}\|_{t_i}^{t_i+p}$ (μm) using moments	$\sigma_d\|_{t_i}^{t_i+p}$ (μm) using moments	$\bar{d}\|_{t_i}^{t_i+p}$ (μm) using Eq. (40)	$\sigma_d\|_{t_i}^{t_i+p}$ (μm) using Eq. (41)	% Deviation of Eq. (40)[a]	% Deviation of Eq. (41)[b]
For $n=1$ zones						
10 to 10	0.1262	0.01813	0.1330	0.01934	5.429	6.646
10 to 11	0.1326	0.01861	0.1397	0.01971	5.363	5.942
10 to 14	0.1527	0.02401	0.1596	0.02469	4.565	2.828
10 to 20	0.1926	0.04276	0.1995	0.04299	3.593	0.5496
For the $n=3$ zones						
15 to 15	0.3873	0.02046	0.3681	0.01615	−4.950	−21.07
15 to 16	0.3921	0.01979	0.3722	0.01580	−5.086	−20.14
15 to 19	0.4052	0.02044	0.3836	0.01676	−5.341	−18.02
15 to 25	0.4269	0.02738	0.4042	0.02329	−5.312	−14.96

[a] Deviation from the moment treatment given in the 2nd column.
[b] Deviation from the moment treatment given in the 3rd column.

$$\bar{f} = \frac{1}{t_{i+p} - t_i} \int_{t_i}^{t_{i+p}} \mathrm{f}(t)\, \mathrm{d}t \tag{37}$$

The average diameter can thus be written as:

$$\bar{d}\big|_{t_i}^{t_{i+p}} = \frac{1}{t_{i+p} - t_i} \int_{t_i}^{t_{i+p}} d(t)\, \mathrm{d}t \tag{38}$$

If we combine $R = t_0/t_r$, the approximation $R = 6\lambda$, and Eq. (3), then the diameter can be expressed explicitly as a function of time such that

$$d(t) = \left(\frac{6t\lambda'}{t_0} \right)^{1/n} \tag{39}$$

Substitution of Eq. (39) into Eq. (38) yields after integrating:

$$\bar{d}\big|_{t_i}^{t_{i+p}} = \frac{1}{t_{i+p} - t_i} \left[\frac{6\lambda'}{t_0} \right]^{1/n} \frac{1}{1 + 1/n} \left\{ t_{i+p}^{(1+1/n)} - t_i^{(1+1/n)} \right\} \tag{40}$$

The analytical treatment for the standard deviation (equal to the square root of the variance or second moment), $\sigma_d|_{t_i}^{t_{i+p}}$, of the fraction collected between times t_i and t_{i+p}} is developed as follows. For $n = 1$ systems, σ_d is time invariant, as discussed above. Hence the response of collecting a zone between times t_i and t_{i+p} can be considered a linear convolution [35,36] of the window function, $W(t_i, t_{i+p})$, and σ_d. The window function $W(t_i, t_{i+p}) = 0$ except in the region $t_i \leq t \leq t_{i+p}$ where $W(t_i, t_{i+p}) = 1$. The window function represents the finite collection time of the eluting zone. For time-invariant functions which have been convolved, the total variance of the convolution product is the sum of the individual function variances [35,36]. Hence,

$$\sigma_d|_{t_i}^{t_{i+p}} = \sqrt{\sigma_d^2 + \sigma_{ft}^2} \tag{41}$$

where σ_{ft}^2 is the variance of the finite sampling window which is known [37] to be equal to $(t_{i+p} - t_i)^2/12$.

This treatment is more approximate for the $n \neq 1$ cases because the broadening will no longer be time invariant, as discussed above, and as seen in Figs. 6 and 7. This means that the simple sum of variances discussed above has a more complex meaning and is much more difficult to obtain analytically. For the $n = 3$ case one can take the average of σ_d between the two time limits, as given in Eq. (37), and use that value for σ_d, which will be shown shortly. In some respects, it may be possible to analytically derive a better approximation for σ_d when $n = 3$ for finite accumulation times. However, it is so simple and fast to just use a computer program which calculates a moment analysis on row sums of the time–size matrix that it hardly seems worth the effort to dwell on approximations of this kind unless they produce insight into the separation process. In addition, the computer program approach allows one to insert an experimental particle size density function in place of the uniform density used as the basis for the outlet polydispersity. In this manner, one can model a real fractionation process without deriving equations that pertain only to a unique size distribution and examine the resulting size density when finite collection times are utilized.

Substituting Eq. (36), which gives σ_d as a function of time for the $n = 3$ case into Eq. (37) yields an average σ_d as:

$$\bar{\sigma}_d\big|_{t_i}^{t_{i+p}} = \frac{wt_0}{3(t_{i+p} - t_i)} \left(\frac{2\pi\eta\langle v \rangle \lambda'}{Lk_B T} \right)^{1/2} \ln \left(\frac{t_{i+p}}{t_i} \right) \tag{42}$$

This will be used in Eq. (41) for the time-variant $n = 3$ case.

The results of Eqs. (40) and (41) are given in Table 1 along with the calculations given more directly by the moment analysis of the summed time–size matrix given in Eq. (27). As can be seen from the numbers for the $n = 1$ case there is good correspondence between the simple theory given by these equations and the computed moments. The percentage deviations shown in Table 1 indicate that agreement gets better between the calculated moment approach and Eq. (41) as the sampling time increases for the $n = 1$ case. This is because the term in Eq. (41) which contains the width of the collection duration, σ_{ft}^2, is more heavily weighted for large collection times and is more accurate than σ_d from Eq. (34). Both the mean diameter and zone width analytical estimates for the $n = 1$ case are predicted to be accurate typically at the 5% level, which is useful when fraction collection is needed.

The results given in Table 1 for the $n = 3$ case

shows a similar accuracy level for the mean diameter. However, the zone width, as measured by the standard deviation, shows a more severe degradation in accuracy as compared to the $n=1$ case. Again, results get better for a larger collection time window. Notice also that for $n=3$ there is a reduction in σ_d as the collection time increases from 0 to 1 min, as shown in Table 1. This is because the inherent zone width shown in Fig. 6 decreases with time so that at longer retention times zones become narrower. This trend is reflected in both the standard deviation calculated from moments analysis and in the analytical theory for the $n=3$ case given in Table 1.

2.7. Programmed fields and other quality criteria

From the results given in Fig. 6 and from other results where the $n=3$ case is discussed, it appears that field programming is necessary to compress the elution range of sedimentation FFF so that smaller particles have more selectivity and larger particles have less selectivity. This point has been recognized previously in FFF studies [29,30] and is one reason why interest in field programming continues.

The use of analytical theory for determining particle size from fast programmed field experiments is known to give large error due to finite zone relaxation times [38]. However, simulation methods [39] can be easily incorporated into the calculation of the time–size matrix for programmed field FFF [38]. Fast multiprocessor workstations can calculate high-resolution time–size matrices with a few hours of computer time. It is this approach that we have utilized in the continued study of this problem for programmed field modes of operation [33].

The apparent and outlet polydispersity and the time–size matrix concepts that have been discussed in this paper complement other metrics such as the fractionating power [29,30] and the specific resolution factor [31] that have been used in other studies of FFF methodology. In this regard, the time–size matrix gives a very visual view of the fractionation process and allows various optimization criteria for field programming with techniques like those where $n\neq1$ need to be viewed visually. It can be expected that these polydispersity metrics will be further utilized in the development of modern FFF methodology.

3. Symbols

$\mathbf{A}_{ij}$	Time–size number density matrix
A, b, C	Constants in the diffusion coefficient equation for polymers
$C_j(\theta)$	Optical extinction coefficient as a function of d_j and θ
D	Diffusion coefficient
d, d_i, d_j, d'	Particle diameter
$d(t)$	Particle diameter as a function of time
$\underline{d}\big\|_{t_i}$	First moment of $N(d_j)$ at time t_i
$\underline{d}\big\|_{t_i}^{t_{i+p}}$	First moment of $N(d_j)$ or average diameter for zones collected between times t_i and t_{i+p}
d_{max}	Maximum particle diameter used in $\mathbf{A}_{ij}$
$\underline{F}$	Flow-rate
$\bar{f}$	Average value of f(t)
f(t)	A general time-varying function
f(t_i, θ)	Detector signal as a function of time t and θ
H	Total plate height
H_{ne}	Plate height due to non-equilibrium
i	Matrix row number index
j	Matrix column number index
k	Number of columns in $\mathbf{A}_{ij}$
k_B	Boltzmann's constant
L	Channel length
M	Molecular mass
m	Number of rows in $\mathbf{A}_{ij}$
$N(d_j)$	Particle diameter number density function
$N(d_j)\big\|_{t_i}$	Particle diameter number density function at constant time
$N(d_j)\big\|_{t_i}^{t_{i+p}}$	Particle diameter number density function for zones collected between times t_i and t_{i+p}
$N(t_i)$	Number of particles at time t_i
n	Integer power of diameter in λ equation
p	Number of matrix rows over which fraction collection takes place
R	Retention ratio
R_{min}	Minimum retention ratio used in the calculations
S_d	Diameter-based selectivity
S_M	Molecular weight-based selectivity
T	Absolute temperature

t	Time
t_r	Retention time
t_0	Void time
t_j'	Retention time obtained through back calculation from d_j
$\langle v \rangle$	Fluid average velocity
$W(t_i, t_{i+p})$	Window function
w	Channel width
x	The transverse coordinate of the channel
z	The axial coordinate of the channel
η	Viscosity
θ	Incident angle of scattered light
λ	Non-dimensional mean layer thickness
λ'	λd^n
λ_{min}	The minimum λ corresponding to d_{min}
σ_{ap}	Standard deviation of the apparent size density function
σ_d	Gaussian standard deviation of particle diameter
σ_j	Time-based Gaussian standard deviation at d_j
$\sigma_d\|_{t_i}$	The standard deviation of $N(d_j)$ at time t_i
$\sigma_d\|_{t_i}^{t_{i+p}}$	The standard deviation of $N(d_j)$ for zones collected between times t_i and t_{i+p}
$\bar{\sigma}_d\|_{t_i}^{t_{i+p}}$	The average standard deviation of $N(d_j)$ for zones collected between times t_i and t_{i+p}
σ_{ft}^2	The zone variance due to finite width time sampling
σ_M	Standard deviation of polymer molecular weight
σ_{ne}	Length-based standard deviation due to non-equilibrium
σ_p	Length-based standard deviation due to polydispersity
χ	Non-dimensional non-equilibrium coefficient

Acknowledgements

I thank Nancy Cohlberg, of Cohlberg Analytical, Blue Bell, PA, USA for editorial assistance and Robert E. Murphy, of the Rohm and Haas Co., Springhouse, PA, USA for assistance in the production of Fig. 10.

References

[1] P.J. Wyatt, Anal. Chim. Acta 272 (1993) 1.
[2] D. Roessner, W.-M. Kulicke, J. Chromatogr. A 687 (1994) 249.
[3] S. Lee, O.-S. Kwon, in: T. Provder, H.G. Barth, M.W. Urban (Eds.), Chromatographic Characterization of Polymers, Hyphenated and Multidimensional Techniques (Advances in Chemistry Series, No. 247), American Chemical Society, Washington, DC, 1995, p. 93.
[4] H. Thielking, D. Roessner, W.-M. Kulicke, Anal. Chem. 67 (1995) 3229.
[5] H. Thielking, W.-M. Kulicke, Anal. Chem. 68 (1996) 1169.
[6] P.J. Wyatt, D.N. Villalpando, Langmuir 13 (1997) 3913.
[7] B. Wittgren, K.-G. Wahlund, J. Chromatogr. A 760 (1997) 205.
[8] P.J. Wyatt, J. Coll. Interface Sci. 197 (1998) 9.
[9] K.D. Caldwell, Anal. Chem. 60 (1988) 959A.
[10] M. Martin, in P.R. Brown and E. Grushka (Eds.), Advances in Chromatography, Marcel Dekker, New York, 1998, Vol. 39, pp. 1–138.
[11] M.E. Schimpf, P.S. Williams, J.C. Giddings, J. Appl. Polym. Sci. 37 (1989) 2059.
[12] M.R. Schure, B.N. Barman, J.C. Giddings, Anal. Chem. 61 (1989) 2735.
[13] M.R. Schure, S.A. Palkar, manuscript in preparation.
[14] M. Kerker, The Scattering of Light and Other Electromagnetic Radiation, Academic Press, New York, 1969.
[15] C.F. Bohren, D.R. Huffman, Absorption and Scattering of Light by Small Particles, Wiley, New York, 1983.
[16] M.E. Hovingh, G.H. Thompson, J.C. Giddings, Anal. Chem. 42 (1970) 195.
[17] M.E. Schimpf, D.D. Russell, J.K. Lewis, J. Liq. Chromatogr. 17 (1994) 3221.
[18] J.C. Giddings, F.J.F. Yang, M.N. Myers, Anal. Chem. 48 (1976) 1126.
[19] J.C. Giddings, F.J.F. Yang, M.N. Myers, Anal. Chem. 46 (1974) 1917.
[20] W.H. Press, S.A. Teukolsky, W.T. Vetterling, B.P. Flannery, Numerical Recipes, Cambridge University Press, New York, 2nd ed., 1992.
[21] J.C. Giddings, L.K. Smith, M.N. Myers, Anal. Chem. 47 (1975) 2389.
[22] J.C. Giddings, J. Chem. Phys. 49 (1968) 81.
[23] J.C. Giddings, Y.H. Yoon, K.D. Caldwell, M.N. Myers, M.E. Hovingh, Sep. Sci. 10 (1975) 447.
[24] R.J. Hunter, Foundations of Colloid Science, Vol. I, Oxford, New York, 1986.
[25] M.R. Schure, Anal. Chem. 60 (1988) 1109.
[26] P.M. Shiundu, G. Liu, J.C. Giddings, Anal. Chem. 67 (1995) 2705.

[27] M.E. Schimpf, J.C. Giddings, Macromolecules 20 (1987) 1561.
[28] J.C. Giddings, K.D. Caldwell, M.N. Myers, Macromolecules 9 (1976) 106.
[29] J.C. Giddings, P.S. Williams, R. Beckett, Anal. Chem. 59 (1987) 28.
[30] P.S. Williams, J.C. Giddings, Anal. Chem. 59 (1987) 2038–2044.
[31] W.W. Yau, J.J. Kirkland, J. Chromatogr. 218 (1981) 217.
[32] M.R. Schure, Sep. Sci. Technol. 22 (1987) 2403.
[33] M.R. Schure, manuscript in preparation.
[34] H. Cramér, Mathematical Methods of Statistics, Princeton University Press, Princeton, NJ, 1974.
[35] R.N. Bracewell, The Fourier Transform and Its Applications, McGraw-Hill, New York, 2nd ed., 1986.
[36] A.V. Oppenheim, R.W. Schafer, Digital Signal Processing, Prentice-Hall, Englewood Cliffs, NJ, 1975.
[37] M. Abramowitz, I.A. Stegun, Handbook of Mathematical Functions With Formulas, Graphs and Mathematical Tables, Dover Publications, New York, 1968.
[38] M.E. Hansen, J.C. Giddings, M.R. Schure, R. Beckett, Anal. Chem. 60 (1988) 1434.
[39] M.R. Schure, in P.R. Brown and E. Grushka (Eds.), Advances in Chromatography, Marcel Dekker, New York, 1998, Vol. 39, pp. 139–200.